Available online at www.sciencedirect.com

ScienceDirect

www.elsevier.com/locate/jmbbm

Research Paper

Preparation of porous bioceramics using reverse thermo-responsive hydrogels in combination with rhBMP-2 carriers: *In vitro* and *in vivo* evaluation

Yin-Chih Fu[a,b,c,d], Chung-Hwan Chen[a,b,c], Chau-Zen Wang[a,e],
Yan-Hsiung Wang[a,f], Je-Ken Chang[a,c], Gwo-Jaw Wang[a,c], Mei-Ling Ho[a,e,*],
Chih-Kuang Wang[a,g,**]

[a]Orthopaedic Research Center, Kaohsiung Medical University, Kaohsiung, Taiwan
[b]Graduate Institute of Medicine, Kaohsiung Medical University, Kaohsiung, Taiwan
[c]Department of Orthopaedics, Kaohsiung Medical University Hospital, Kaohsiung Medical University, Kaohsiung, Taiwan
[d]Department of Orthopaedics, Kaohsiung Municipal Hsiao-Kang Hospital, Kaohsiung Medical University, Kaohsiung, Taiwan
[e]Department of Physiology, Kaohsiung Medical University, Kaohsiung, Taiwan
[f]School of Dentistry, Kaohsiung Medical University, Kaohsiung 807, Taiwan
[g]Department of Medicinal and Applied Chemistry, Kaohsiung Medical University, Kaohsiung, Taiwan

ARTICLE INFO

ABSTRACT

Porous biphasic calcium phosphates (BCP) were fabricated using reverse thermo-responsive hydrogels with hydroxyapatite (HAp) and β-tricalcium (β-TCP) powder and planetary centrifugal mixer. This hydrogel mixture slurry will shrink and compress the HAp powder during the sintering process. The porous bioceramics are expected to have good mechanical properties after sintering at 1200 °C. Reverse thermo-responsive hydrogels of poly[(N-isopropylacrylamide)-co-(methacrylic acid)] p(NiPAAm–MAA) were synthesized by free-radical cross-linking copolymerization, and their chemical properties were evaluated by nuclear magnetic resonance spectroscopy, infrared spectroscopy, and electrospray-ionization mass spectrometry. The lower critical solution temperature (LCST) of the hydrogel was determined using turbidity measurements. A thermogravimetric analysis was used to examine the thermal properties. The porous bioceramic properties were analyzed by X-ray diffraction, scanning electron microscopy, bulk density, compressive strength testing and cytotoxicity. The compressive strength and average porosity of the porous bioceramics were examined at approximately 6.8 MPa and 66% under 10 wt% p(NiPAAm–MAA)=99:1 condition. The ratio of HAp/β-TCP can adjust two different compositional behaviors during the 1200 °C sintering process without resulting in cell toxicity. The (rhBMP-2)-HAp-PLGA carriers were fabricated as in our previous study of the double

emulsion and drop-coating technique. Results of animal study included histological micrographs of the 1-mm defect in the femurs, with the rhBMP-2 carrier group, the bioceramic spacer group and the bioceramic spacer with rhBMP-2 carriers group showing better callus formation around the femur defect site than the control group. The optimal dual effects of the bone growth factors from osteoconductive bioceramics and osteoinductive rhBMP-2 carriers produced better bone formation.

1.   Introduction

Commonly, salvage procedures for bone cancer, comminuted open fractures, and severe atrophic non-unions often cause large bone defects. Because of the lack of an osteoconductive matrix for bone regeneration, these procedures require further surgical treatment. The typical gold-standard treatment is autogenous bone grafts, which require harvesting 'donor' bone from a non-weight-bearing site of the same patient for transplantation into the defect site (Bauer and Muschler, 2000). However, the use of this technique is severely restrained due to limited quantities and the considerable donor site morbidity associated with the harvest (Silber et al., 2003; Lord et al., 1988). Other common sources of bone graft replacements are allografts and xenogeneic bone grafts. However, the disadvantages of allografts and xenogeneic bone grafts are the immune- and disease-related complications (Lord et al., 1988; Muscolo et al., 2006). Many bone substitute materials that were intended to replace the need for autologous or allograft tissue have been evaluated over the last two decades (Hench and Polak, 2002; Kretlow and Mikos, 2007). The current bone formation strategy is that artificially synthesized biomaterials should simultaneously have both osteoinductive and osteoconductive functions, allowing for integration into the surrounding host bone (Stevens, 2008). Depending on the relevant tissue engineering criterion, the ideal basic hypothesis is that the implanted materials will be resorbed and replaced over time by the body's own newly regenerated bone tissue (Langer and Vacanti, 1993). Some studies reported that porous biphasic bioceramics of hydroxyapatite/β-tricalcium phosphate (HAp/β-TCP) can promote osteoconduction during new bone formation in in vivo experiments (Daculsi et al., 2003; Yamada et al., 1997). Furthermore, the resorption rate of this porous bioceramic can be tailored using the HAp/β-TCP ratio so that the bioceramic persists for years following implantation, while other calcium phosphates have a greater capacity to be resorbed (Yamada et al., 1997).

Hulbert et al. indicated that optimal bone tissue ingrowth was found for pore sizes greater than 100 μm due to cell sizes (Daculsi et al., 2003). For migration and transport, the optimal pore size for porous bone substitutes has been explored by many investigators (Hulbert et al., 1970; Stevens, 2008; Uchida et al., 1985). According to the current literature, the optimal pore size is estimated to be 100–600 μm (Hulbert et al., 1970; Uchida et al., 1985). However, the brittle nature of porous bioceramic substitutes cannot match the toughness of bone, which limits the use of these materials for clinical load-bearing applications (Fan et al., 2012). Therefore, the current challenges for the tissue engineering of porous bioceramics are to match both the mechanical and biological context of the real bone tissue matrix and to support the ingrowth of neovascularization and cells (Stevens, 2008). Several technologies exist for manufacturing strong and reliable porous ceramics. These scaffold preparation methods allow one to control the pore sizes and yield scaffolds with interconnected pores and the desired geometry; however, the mechanical strength is often too low to match the compressive strength of cancellous bone (approximately 4–12 MPa) (Gauthier et al., 1999; Huglin et al., 1997; Ramay and Zhang, 2003). Increasing the compressive strength of scaffolds without decreasing the porosity and pore size is a challenge for researchers.

The potential of reverse thermo-responsive hydrogels has been recognized for tissue regeneration because gelation can occur as the temperature increases above the lower critical solution temperature (LCST), which is constructed to be below body temperature (Cui et al., 2007; Gan et al., 2009; Rezwan et al., 2006). The pNiPAAm (poly(N-isopropylacrylamide)) can exhibit gel volume contraction if the temperature increases above the LCST of 32 °C (Fujishige et al., 1989; Heskins and Guillet, 1968). At 32 °C, the induced phase transition of pNiPAAm in aqueous solution may mainly be driven by the thermal destruction of hydrogen bonds between water molecules and hydrophilic groups, such as –CO- and –NH- in the NiPAAm monomer. Furthermore, the interaction between hydrophobic segments on the polymer increases with increased temperature (Hirotsu, 1987; Otake et al., 1990; Solis et al., 2005). Of pNiPAAm-based copolymers, the copolymer poly(N-isopropylacrylamide-co-methacrylic acid) (p(NiPAAm–MAA)) is of special interest because the methacrylic acid (MAA) group introduces additional ionized groups to the copolymer. As a result, the copolymer contains hydrophobic segments and hydrophilic groups and can be useful for the absorbance of metal ions (Tian et al., 2008). Therefore, p(NiPAAm–MAA) hydrogels should be beneficial for the dispersion of hydrophilic and hydrophobic powders. However, a challenge with using pNiPAAm in biomedical applications, such as controlled drug delivery or tissue engineering scaffolds, is that pNiPAAm is not biodegradable, which limits its use in temporary implantation applications.

Considering the above findings, we aimed to fabricate a new scaffold possessing both an even distribution of porosities for cell ingrowth and optimal compressive strength. We hypothesize that the p(NiPAAm–MAA) hydrogel would shrink and compress the HAp powder during sintering as the temperature increases. The porous bioceramics formed using this material would have mechanical properties similar to those of cancellous bone. We also tested the cell cytotoxicity

of this porous bioceramic to prove its safety for clinical applications. Then, we evaluated the new porous bioceramic in vivo and combined our results with those of our previous controlled release of rhBMP-2 microsphere carriers (Wang et al., 2009) to determine that these materials can be used as both osteoconductive and osteoinductive functional bone scaffolds in an atrophic non-union animal model.

2. Materials and methods

2.1. Preparation and characterization of porous bioceramics

Hydroxyapatite (HAp) (CAPTAL®S, Plasma Biotal Limited, US) and β-TCP were used as the main raw materials in this study. Reagent-grade N-isopropylacrylamide (NiPAAm), methacrylic acid (MAA), the activator N,N,N',N'-tetramethylethylenediamine (TEMED), and the initiator ammonium persulfate (APS) were purchased from Sigma-Aldrich, Inc. (US) and were used without any further purification. The other chemicals were of analytical grade and were used without further purification.

Poly[(N-isopropylacrylamide)-co-(methacrylic acid)] (p(NiPAAm–MAA)) was synthesized by free-radical cross-linking copolymerization in a solution of 99 mol% NiPAAm and 1 mol% MAA (PNM99:1); the main parameters were as described previously (Tian et al., 2008). Briefly, the target amount of 5 g of NiPAAm and 40 μl of MAA were added to 25 mL of deionized water in a 100 mL reactor. The solution was stirred for 1 h, deoxygenated by bubbling with nitrogen for 40 min, and finally heated to 50 °C in a nitrogen environment. Then, 500 μl of TEMED and 0.05 g of APS were added to the reactor to initiate polymerization. The reaction was maintained at 50 °C under a nitrogen atmosphere for 24 h with constant stirring. The p(NiPAAm–MAA)=99:1 (PNM99:1) hydrogel that formed was then purified by membrane dialysis against distilled deionized water using a Spectra/Pros membrane with a molecular weight cutoff (MWCO) of 1000. The sample was then freeze-dried to form a white powder. The purified copolymer was characterized as described. ^{1}H –NMR spectra were recorded on a nuclear magnetic resonance spectrometer (Varian Gemini-200, US), and the sample was dissolved in D_2O. Molecular weights were determined using ESI-MS on a quadrupole TOF mass spectrometer (Bruker BioTOF Q, US). The LCST of the hydrogel was determined using turbidity measurements. The turbidity of the polymer solution was measured at 500 nm using a UV/VIS/NIR spectrometer (JASCO V570, Japan) equipped with a temperature controller. Thermo-gelling was evaluated for the aqueous 30 wt% PNM99:1 hydrogel first. The shrinkage ratio, $[(D_0–D_S)/D_0] \times 100\%$, is defined as the ratio of the difference in diameters between the original and shrunken hydrogel to the original diameter of the hydrogel, where D_0 is the original diameter of the hydrogel, and D_S is the diameter of the hydrogel after shrinkage at each temperature. Thermogravimetric analysis (TGA; Perkin–Elmer Pyris-Diamond thermogravimetric analyzer, US) was used to examine the thermal properties of the PNM99:1 sample and to determine the sintering temperature. The TGA analysis was performed using a 5 mg sample under a nitrogen gas atmosphere in platinum crucibles. The scan rate was 10 °C/min from 25 to 800 °C.

The porous bioceramics were prepared using aqueous solutions containing 2 ml of 0, 10, 15 and 20 wt% PNM99:1 hydrogel mixed with 2 g of HAp to form a ceramic slurry using a planetary centrifugal mixer at 1000 rpm for 2 min (Thinky Mixer AR-100, Thinky, Japan). The ceramic slurry was then poured into an Al_2O_3 mold and dried to form a green cylinder with a diameter of 6.0 ± 0.1 mm and a height of 12.0 ± 0.1 mm. The green cylinder was slowly heated (in a Nabertherm HTC-03/14 electrical furnace (German) in an air atmosphere) to 600 °C for 1.5 h, and the temperature was then maintained at 600 °C for 30 min. Next, the temperature was increased to 1200 °C over 30 min and kept at that temperature for 30 min, followed by cooling to room temperature. The porous chunk that was obtained was cut into smaller pieces using a diamond saw to produce the desired shapes. X-ray diffraction (XRD; Rigaku D/max VIII, Japan) with CuKα radiation was used to characterize the phase composition of the bioceramics. Microstructure observations of the bioceramic samples were performed using an optical camera and scanning electron microscopy (SEM; Hitachi SU8000, Japan). The bulk density of the complex geometric parts and their various porosities were determined using the ASTM procedure C373, which is based on Archimedes' principle. We also recorded three-section images of each type of porous bioceramic sample using a microscopic camera (MICROTECH Mini Scope-V, M&T OPTICS CO., Taiwan). Subsequently, we analyzed the pore size and area percentage using Feret's diameter method in ImageJ software. Liquid permeability experiments were performed using blue ink, which was slowly added dropwise on the top surface of the columnar porous bioceramics. Compressive strength tests were also performed using the ASTM procedure C773-88, and the compressive strength can be calculated using the following formula: $\sigma=F/A$ (F=load at fracture and A=area of the disc surface). The specimens used for compression testing were usually cylinders with a height to diameter ratio of 2:1. Specimens with a diameter of 5.7 ± 0.2 mm and a height of 11.7 ± 0.2 mm were loaded at a crosshead speed of 0.5 mm/min (Instron 4400, Instron Corp., US). Six samples of each group were used for a statistical analysis. All the porosity and strength data were statistically analyzed and expressed as the mean$\pm$standard deviation (SD).

2.2. Preparation of (rhBMP-2)-HAp-PLGA carriers

The rhBMP-2 carriers were microspheres (size range: 10 μm–120 μm) synthesized using our previously described technique (Wang et al., 2009), in which the main components are poly (D,L-lactide-co-glycolide) (PLGA65/35; Sigma-Aldrich, US) and hydroxyapatite (HAp; Alfa Aesar®, A Johnson Matthey Company, US). Briefly, 250 μl of a PBS (phosphate-buffered saline) buffer solution acted as the first water-phase suspension. Then, 250 mg of the PLGA65/35 was dissolved in 2.5 ml of dichloromethane to form a 10% PLGA oil-phase solution. The first water-phase solution and the 10% PLGA were mixed at 1000 rpm for 15 min to form the first water-in-oil (w/o) microemulsion. The first microemulsion (w/o) was added to 10 ml of the 0.1% (w/v) polyvinyl alcohol (PVA) (PB-05,

Chang Chun Petrochemical Co., Taiwan) second water-phase solution and then stirred at 350 rpm for 4 h to form a second microemulsion (W/O/W), eliminate the dichloromethane and solidify the microspheres. These microspheres were collected by centrifugation, washed with distilled water and lyophilized. Finally, to effectively adjust the concentration of released rhBMP-2, the surfaces of the 50 mg lyophilized microspheres were coated with a solution of 60 µl of PBS, 200 µg of rhBMP-2 (2000 ng, CHO-expressed; Catalog: 355-BM; R&D systems, US) and 2 mg of HAp powder.

2.3. Cell viability of the porous bioceramic

In vitro tests were used for screening purposes, according to ISO 10993–5. MC 3T3-E1 osteoblast-like cells were cultivated in Dulbecco's modified Eagle's medium (DMEM) containing 10% fetal calf serum (FCS), 0.01% ascorbic acid, nonessential amino acids and 100 U/ml penicillin/streptomycin (Gibco-BRL; Grand Island, US) at 37 °C in a humidified incubator containing 5 vol% CO_2. The culture medium was replenished every other day; for subculture, the cell monolayer was rinsed with PBS and detached by incubation with trypsin-EDTA (0.25 wt%) for 5 min at 37 °C. Changes in the cell viability of the MC 3T3-E1 cells were quantitatively assessed with a tetrazolium compound (MTS; Sigma, US) for 24 and 48 h culture periods. In the presence of phenazine methosulfate (PMS), this tetrazolium compound, 3-(4,5-dimethylthiazol-2-yl)-5-(3-carboxymethoxyphenyl)-2-(4-sulfophenyl)-2 H-tetrazolium, inner salt (MTS), resulted in a water-soluble formazan product that had an absorbance maximum at 550 nm in PBS. The amount of colored product formed was proportional to the number of cells and to the incubation time of the cells with MTS/PMS. To indirectly evaluate the viability of cells that contacted the material, 5000 cells per well were seeded in a 96-well two-dimensional cell culture plate and cultured at 37 °C in a humidified incubator containing 5 vol% CO_2. The dissolution extracts were prepared by adding the culture medium to porous bioceramics (0.2 g/ml) that had previously been incubated in DMEM at 37 °C for 24 h and sterilized by 260 nm UV light. Conventional Al_2O_3 that had also been incubated in DMEM at 37 °C for 24 h in the medium (0.02 g/ml) at 37 °C for 24 h was used as a negative control. Phenol diluents (0.3%) were used as a positive control and were placed into each well (100 µl/well) and cultured at 37 °C in a humidified incubator containing 5 vol% CO_2. The culture plates without samples were used as normal controls. After 24 and 48 h of cultivation, 10 µl of MTS solution (5 mg/ml in PBS) was added to each well and incubated for another 4 h (37 °C). The optical density (OD) of the water-soluble formazan produced in the solution was measured using an ELISA reader (SLT, Crailheim, Germany). The data were collected and averaged from the five different wells per condition. The data were plotted as the mean±standard deviation (SD) ($n=3$).

2.4. Experimental animals and surgical technique

All procedures were performed in accordance with the specifications in the Guidelines for Animal Experiments of Kaohsiung Medical University. Balb/C mice were anesthetized by an intraperitoneal injection (3.2 mg/30 g body weight) of ketamine (Ketalar®, Parke-Davis, New Zealand) in combination with a 3.7 mg/30 g body weight dose of thiazine-hydrochloride (Rompun®, Bayer HealthCare, Germany). In the non-union animal model, we created a 1 mm gap with a saw in the mid-part of the femur on the right side of a Balb/C mouse. Before surgery, the porous bioceramic samples were first sterilized using dry heat at 80 °C for 24 h. In addition, the rhBMP-2 carriers were produced using a sterile process, as far as possible, and then sterilized using 260 nm UV overnight in this study. A porous bioceramic spacer that was 2 mm in diameter and 1 mm thick was placed in the gap, and both ends of the bone were fixed with a Π-shaped pin. (rhBMP-2)-HAp-PLGA carriers (Wang et al., 2009) were placed beside the bioceramic spacer, and the wound was closed with 4–0 silk sutures. These mice were divided into four groups: the control group, the rhBMP-2 carrier group, the bioceramic spacer group and the bioceramic spacer with rhBMP-2 carriers groups. An empty bone defect without any scaffold was regarded as the control group. For the rhBMP-2 carrier surgical procedures, 5 mg of carrier (carrying approximately 200 ng of rhBMP-2) was compressed into one piece and then placed either beside the porous bioceramic disc or into the bone defect site alone for the rhBMP-2 group. Twelve mice in each experimental group were utilized independently and divided into two observation periods for the 6th and 8th weeks after surgery (6 mice in each observation period).

2.4.1. Soft X-ray observation
At 0, 6 and 8 weeks after the operation, the femur fractures were radiographically examined using soft X-rays (SOFTEX, Model M-100, Japan) at 43 KVP and 2 mA for 1.5 s. The appropriate magnification was applied throughout the observation period, and the resultant micrographs were compared among all scaffolds and with the controls.

2.4.2. Histological analysis and immunostaining of bone tissue
Histochemical and immunohistochemical analyses were concurrently employed to assess the microscopic changes in the bone tissue as a supplement to the X-ray observation. Prior to hematoxylin-eosin (H&E) and immunohistochemical (IHC) staining, all samples of bone tissue were decalcified [0.5 M EDTA-$2H_2O$ in DDW (186. 1 g/L)] for 2 weeks followed by fixation with 4% paraformaldehyde. The resultant samples were embedded into paraffin wax, and 5 µm sections were prepared. The sections were routinely stained with H&E and observed using a microscope at $40\times$ and $100\times$ magnification. Under $40\times$ magnification, we defined the counted callus area as the area within 1 mm proximally and distally to both fracture ends. The callus area around the graft was measured using Image-Pro Plus 5.0 software (Media Cybernetics Inc., US). The percentage of bone matrix within the callus was calculated and compared with that of the control group. IHC staining of endothelial vessels for von Willebrand factor (vWF) was performed as follows. The sections were treated for 9 min with 0.15 mg/L of trypsin in phosphate buffer at pH 7.8 and then incubated overnight at 4 °C with a 1:300 dilution of polyclonal rabbit antihuman vWF antibody (CHE-MICON International, Inc., US). Goat anti-rabbit biotinylated

immunoglobulin (DakoCytomation, Denmark) was used at a 1:300 dilution as the secondary antibody for 60 min at 37 °C. An avidin–biotin–peroxidase complex (Vector Laboratories, Burlingame, US) was applied at a 1:300 dilution for 60 min at 37 °C. The peroxidase activity was detected using 0.4 mg/L of 3,3''-diaminobenzidine in phosphate buffer at pH 7.3 in the presence of 0.12% H_2O_2. The sections were then counterstained with hematoxylin.

2.4.3. Statistical analysis

All the callus formation scoring data were statistically analyzed to express the mean$\pm$SD ($n=6$). A one-way ANOVA was performed, and the $*p<0.001$ and $**p<0.0001$ were compared to the control or compared between treatment groups.

3. Results and discussion

3.1. p(NiPAAm–MAA) copolymer synthesis

The ^{1}H–NMR results, shown in Fig. 1(a) and (b), show the NiPAAm monomer and PNM99:1 copolymer. The peak attributed to the methyl group in the NiPAAm monomer appeared at 1.1 ppm, and the isopropyl C−H signal was present at 3.9 ppm. In addition, the double-bond peaks of the NiPAAm monomer were observed at 5.7 ppm and disappeared at 6.1 ppm. The structure of the PNM99:1 copolymer was also supported by the ^{1}H–NMR, as shown in Fig. 1(b). These data contain two broad peaks (−CH−CH$_2$−) at 1.4 and 1.9 ppm, a peak (−CH$_3$) due to the isopropyl group at 1.0 ppm, and a peak (−NH−CH−) at 3.8 ppm that was attributed to the hydrogen proton of the pNiPAAm units of the chain. The minor MAA units of the copolymer showed that the intensity of the

Fig. 1 – ^{1}H NMR spectrum of NiPAAm monomer and p(NiPAAm-co-MAA)=99:1 (PNM99:1) copolymer.

methyl group was significantly enhanced due to the introduction of the methyl group of pNiPAAm (chemical shift at 1.2 ppm) (Rafie et al., 2012). However, the double-bond peaks of the NiPAAm monomer observed at 5.7 ppm and 6.1 ppm disappeared. The FTIR result shown in Fig. S1 of the supporting information also indicated successful polymerization of NiPAAm and MAA, as expected. The molecular weight of the PNM99:1 copolymer as analyzed by LC-mass spectrometry was approximately 1000 (mass spectrum (ESI): m/z 1060 (M)$^+$) (Fig. S2 of supporting information).

3.2. Temperature dependent thermo-gelling and thermogravimetric analysis

Fig. S3 of the supporting information demonstrates that the 30% PNM99:1 hydrogel showed a transition at temperatures between 32.5 °C and 34.1 °C. As the temperature increased above 34.1 °C, a white dispersion was formed. Similar phase transition temperatures (33.0 °C–35.0 °C) were also observed for the 30% PNM97:3 (p(NiPAAm–MAA)=97:3) hydrogel. As the literature reports (Zhang et al., 2004), at temperatures below the LCST, pNiPAAm hydrogels show water-swollen properties due to the hydrogen bond interactions between water and the hydrophilic amide groups of the polymer. At temperatures near or higher than the LCST, hydrophobic interactions between the isopropyl pendant groups increase, and the hydrogels appear to be hydrophobic; the pNiPAAm starts to aggregate, and phase separation occurs. In addition, Feil et al. reported (Feil et al., 1993) that the presence of hydrophilic moieties in polymer networks containing NiPAAm caused an increase in the LCST value in comparison with the value found with pNiPAAm. Therefore, the phase transition temperature increased as the MAA content increased. This change is because the increased hydrophilicity of the copolymer resulted in an increase in the phase transition temperature.

The key point is that reverse thermo-responsive hydrogels containing pNiPAAm and p(NiPAAm–MAA) can decrease their volume when the temperature is increased. Fig. 2 shows photographs of aqueous 30 wt% PNM99:1 hydrogels taken at different temperatures and stages of shrinkage. The diameter size ratio of the 30% PNM99:1 hydrogel decreased from 100% to 25% when the temperature increased from 25 °C to 300 °C. This hydrogel ratio decreased by nearly 75% as the temperature gradually increased to 300 °C, which indicates that the shrinking volume size of the PNM99:1 induced compression of all the components in response to high temperature. This phenomenon can be regarded as functioning in a manner similar to the cold isostatic press (CIP) step before the powder sintering densification process. In other words, the reverse thermo-responsive hydrogel can evenly mix with HAp powder, and the volume of this hydrogel mixture will shrink and compress the HAp powder as the sintering temperature increases. Finally, sintering densification is expected via free volume contraction, which will increase the mechanical properties after the formation of the porous bioceramics. TGA was used for the thermal analysis of the polymers to determine the burn-out temperature during the sintering process. Fig. S4 of the supporting information shows the thermograms of the PNM99:1 polymer in the temperature
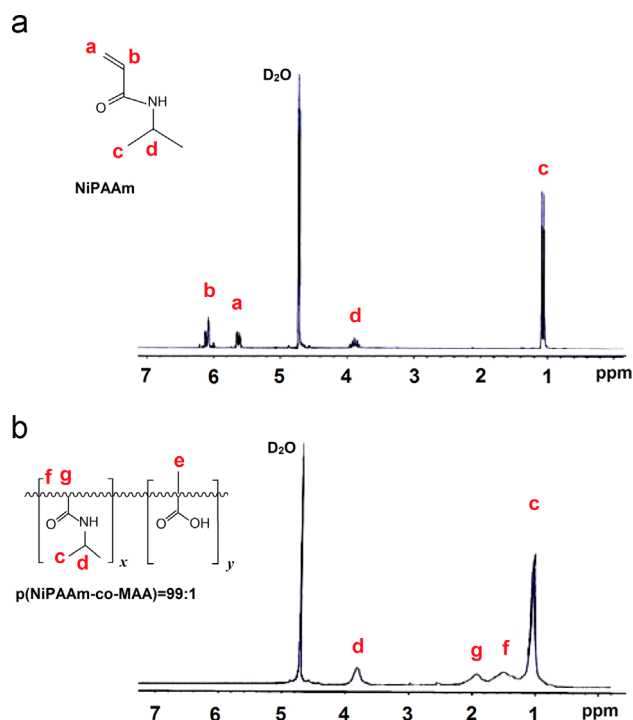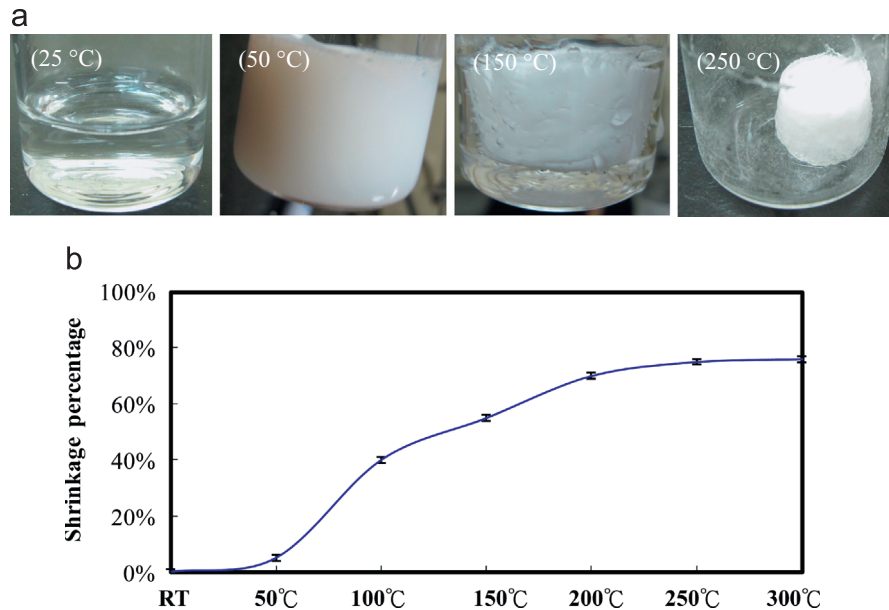
a

b

Fig. 2 – The change of PNM99:1 hydrogel in the appearance, as shown in optical microphotographs (a), and shrinkage ratio of PNM99:1 hydrogel in diameter (b).

range from room temperature to above 560 °C. The complete burn-out temperature of PNM99:1 is clearly located at 600 °C. Therefore, the slurry mixture of PNM99:1 polymer and HAp powder was slowly heated to 600 °C over 1.5 h and maintained at 600 °C for 30 min to result in shrinkage and then burn-out.

3.3.   Characterization of the porous bioceramic

Fig. 3(a) shows the porous bioceramic samples of various concentrations of PNM99:1 hydrogel after 1200 °C sintering. These PNM99:1 hydrogels can act as a binder template for preparing a high integrity porous bioceramic (ϕ: 5.7$\pm$0.2 mm/ height: 11.7$\pm$0.2 mm); i.e., they do not have cracks or easily released particles. The morphology of different concentrations of the PNM99:1 hydrogel and HAp slurry on porous bodies after 1200 °C sintering is shown in Fig. 3(b–f) using SEM images. The macropore structure and distribution are also shown. These macropores can be greater than 300–500 μm, and smaller pore sizes of 100–300 μm are also present. Those macropores (100–500 μm) should also come from the air bubbles generated during the mixing process because air bubbles are known to be entrapped when viscous fluids are stirred using mechanical force; the plastic viscosity decreased with increasing air content (Rust and Manga, 2002). From the results of the pore size and pore area percentage analysis (Fig. S5 of the supporting information) showed the bioceramic product that was fabricated without PNM99:1 hydrogel was unlikely to cause pores larger than 100 μm. In contrast, a range of pore sizes was easy to obtain for the porous bioceramics that were fabricated from 10–20% PNM99:1 hydrogel solutions. For example, three intervals of pore areas (100–300 μm, 300–500 μm and 500–700 μm) accounted for approximately 34–42%, 22–28% and 21–23%, respectively, of the overall pore area from the 100–1000 μm pore range (Fig. S5 (e)). An optimal pore size exists for successful cell infiltration

and bone tissue ingrowth: 100–350 μm for bone tissues (Komlev and Barinov, 2002). Moreover, reports (Hulbert et al., 1970; Stevens, 2008; Uchida et al., 1985) indicated that pores of sizes between 100 and 1000 μm play an important role in cellular and bone ingrowth, being necessary for blood flow distribution. This finding indicated that the porous bioceramic products that were fabricated using this new method have a suitable pore size range (100–1000 μm) for the growth of bone and blood vessels.

The magnified morphologies of porous bodies with different concentrations of the PNM99:1 hydrogel slurry after 1200 °C sintering are also shown in Fig. 4(a–e) using SEM images. We supposed that these crevices formed due to residual space in the PNM99:1 polymer after burn-out at high temperatures. In addition, the minimum crevices (<5–100 μm) should be attributed to a lack of sintering densification. A characteristic of similar methods is the potential for a wide variation in porosity and pore size by using different templates, which act as porogens within the ceramic (Dong et al., 2001; Tadic et al., 2004; Tampieri et al., 2001). However, calcination is often required to remove these organic templates. The grain sizes are on the order of a micrometer, and most of the individual granular HAp particles are sintered and coalesced. The current methods to introduce porosity into a bioceramic are mainly based on the admixture of a combustible reverse thermo-responsive hydrogel that burns away during sintering and on the air bubbles generated during the mixing process that leave free spaces in the resulting object. However, macropore formation from polymer porogens and induced air bubbles in the slurry method usually lead to closed pores that are connected by small-diameter connecting channels only, i.e., not to an obvious interconnecting, bone-like pore network. Liquid permeability tests were performed to understand whether these crevices have liquid permeability and whether those large pores have interconnection channels. The liquid permeability results of
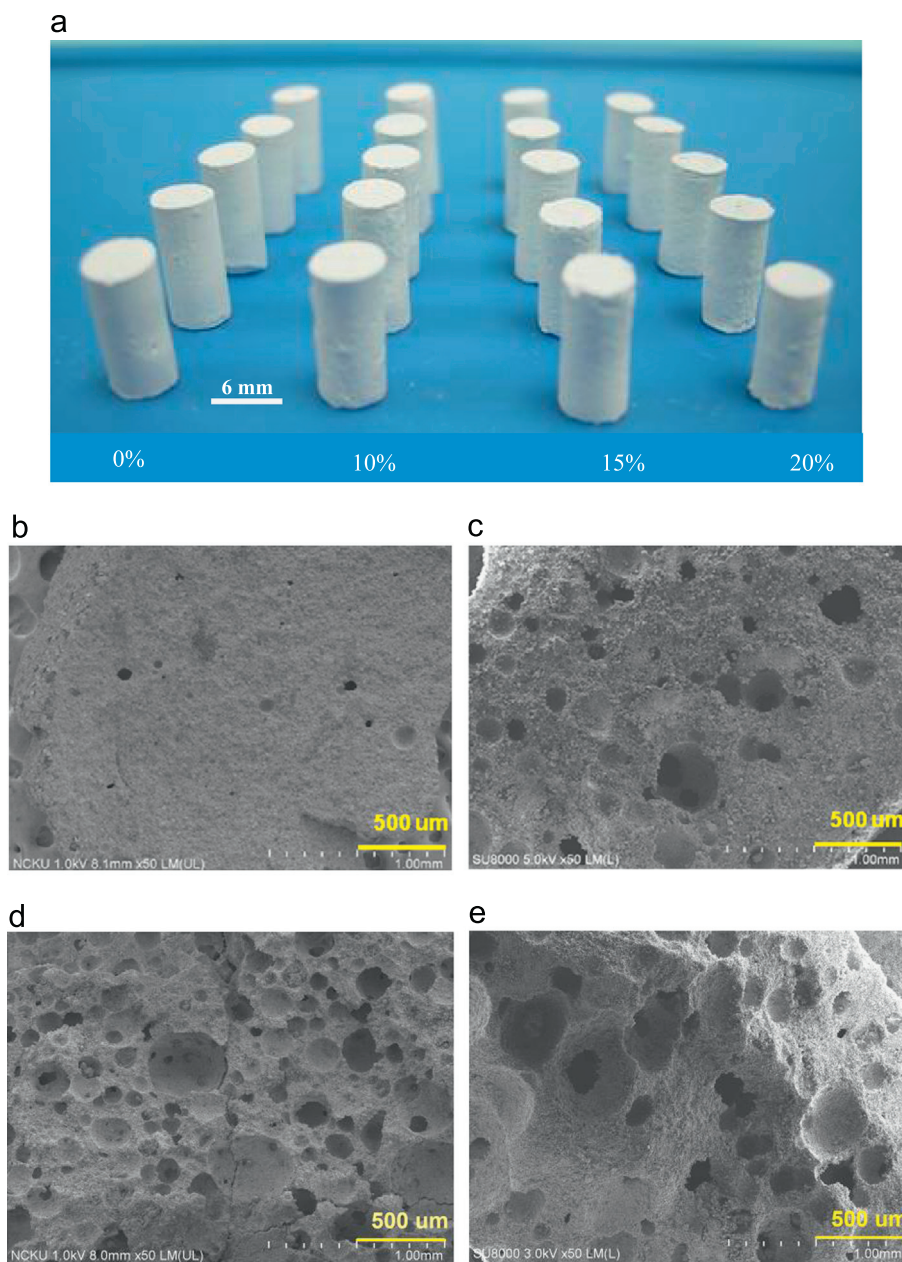
Fig. 3 – Optical photograph (a) and SEM micrographs (× 50; b–f) of whole block of porous HAp/β-TCP (6/4) bioceramics with different concentrations of PNM99:1 hydrogel.

Fig. S6 showed that blue ink will permeate through the whole body of a porous bioceramic because the 80 μl of blue ink was slowly added dropwise to the top surface of a columnar porous bioceramic. Therefore, a porous bioceramic fabricated using this type of new method will allow the movement of nutrients or metabolites when implanted in animals. Furthermore, an alternative route is to create different ratios of biphasic bioceramics from HAp and β-TCP, and then the more highly soluble β-TCP can be dissolved to help produce interconnecting pores.

Fig. 5 shows the dependence of porosity and compressive strength on the four concentrations of PNM99:1 hydrogel. The calculations were performed within the range of 0 wt%, 10 wt%, 15 wt% and 20 wt% PNM99:1 hydrogel. When the concentration of PNM99:1 hydrogel was increased, the porosity

also increased by 47.6%, 66.2%, 68.4% and 65.2%, respectively, but the porosity of the 15 wt% PNM99:1 was even greater than that of the 20 wt% PNM99:1. The difference may result from the coordination of three factors, air bubbles, PNM99:1 polymer residual space, and sintering densification via free volume contraction, because the relative density plays an important role in determining the mechanical properties of porous ceramics. The advantage of high-porosity scaffolds for achieving a good cellular distribution has been reported, and it is critical to select the correct pore size (Solchaga et al., 1999). However, few methods can completely satisfy all the necessary porous bioceramic requirements, namely, a controlled level of high porosity combined with good mechanical properties. Thus, porosity can adversely affect the important mechanical characteristics of a scaffold. Therefore, the
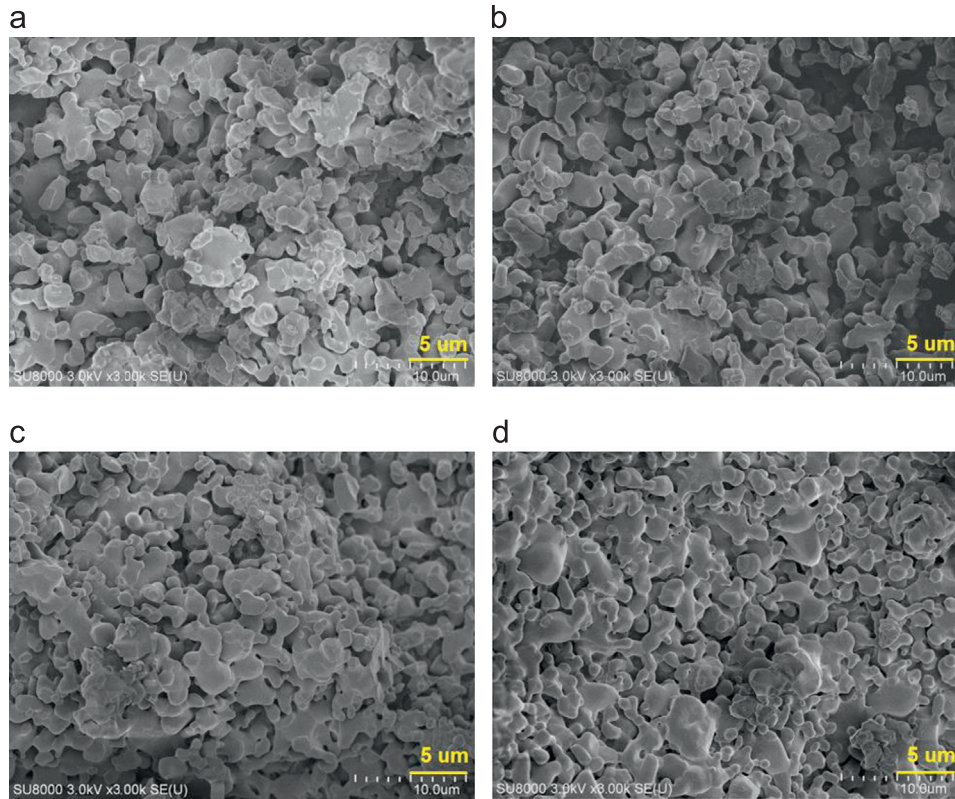
Fig. 4 – SEM micrographs ($\times$ 3000; a–d) of whole block of porous HAp/β-TCP (6/4) bioceramics with different concentrations of PNM99:1 hydrogel.
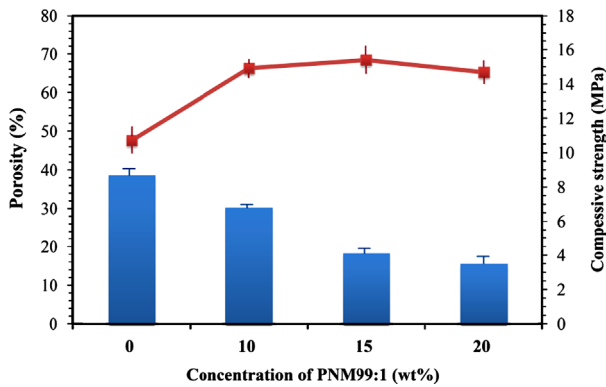

Fig. 5 – Porosity and compressive strength of the porous HAp/β-TCP (6/4) bioceramics after 1200 °C sintered.

Fig. 6 – XRD patterns of the porous HAp/β-TCP (6/4) bioceramics after 1200 °C sintered, commercial HAp and β-TCP. ($\beta = \beta$-TCP, H $=$ HAp).

compressive strength of these materials depends on the compressive strength of cancellous bone, which has been reported to be in the range 4–12 MPa (Gauthier et al., 1999; Huglin et al., 1997; Ramay and Zhang, 2003). The compressive strength of these porous bioceramics was examined at 8.7 MPa, 6.8 MPa, 4.1 MPa and 3.5 MPa for the range of 0 wt%, 10 wt%, 15 wt% and 20 wt% PNM99:1 hydrogel, respectively (Fig. 5). Han et al. reported that the porosity and grain contacting area are two key factors affecting the strength of ceramic foams (Han et al., 2002). The phenomenon of the compression strength being higher at a porosity of 15 wt% PNM99:1 than at a porosity of 20 wt% PNM99:1 should result from the grain contacting area. Of course, the mechanical
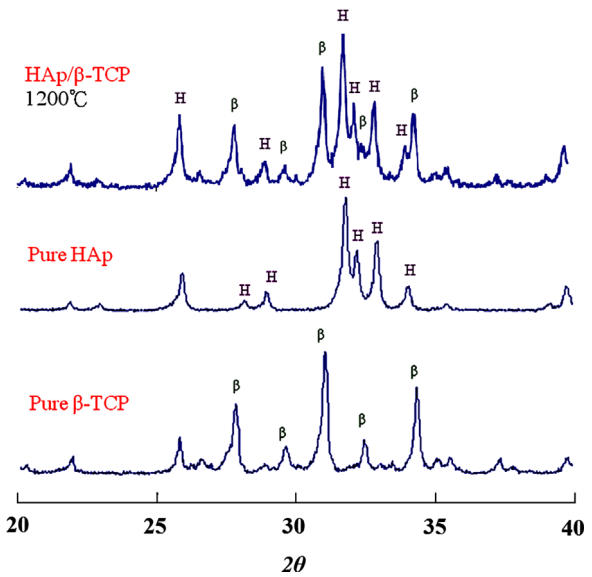
stability should decrease for increased porosity. However, there the compressive strength does not significantly increase with increasing relative density in this case. Thus, the reverse thermo-responsive hydrogel can be regarded as acting like a cold isostatic press (CIP) before the powder sintering processing to shrink and compress the HAp powder,

Table 1 – Phase analysis of porous bioceramics by XRD spectrum.

Naming	HAp+β-TCP raw materials (g)	β-TCP raw materials (wt%)	P99N1M* (wt%) (1 ml)	HAp/β-TCP phase ratio before 1200 °C sintered[a] (%)	HAp/β-TCP phase ratio after 1200 °C sintered[a] (%)
HAp/β-TCP (7/3)	2.0	0	15	100	65
HAp/β-TCP (6/4)	2.0	20	15	79	59
HAp/β-TCP (4/6)	2.0	30	15	66	41
HAp/β-TCP (3/7)	2.0	40	15	62	29

* P99N1M is p(NiPAAm–MAA)=99:1.
[a] The phase ratio (%) refers to the HAp/β-TCP phase ratio of the peak areas by XRD compared with actual weight ratio.

strengthening the mechanical properties. Therefore, the variation in compressive stress using this novel reverse thermo-responsive hydrogel method is due to the porosity, pore distribution and densification of the ceramic skeleton.

Fig. 6 shows the XRD patterns of the slurry after sintering at 1200 °C. The XRD peaks of all of the diffraction patterns agree well with those of standard HAp and β-TCP in the powder diffraction file (Card no. 9-432 and 9-169). A phase calibration curve of the XRD spectrum was prepared using standard HAp and β-TCP, and different HAp/β-TCP phase weight ratios can be found in Table 1. Table 1 shows the HAp/β-TCP phase weight ratio of porous bioceramics at 65/35, 59/41, 41/59 and 29/71 following different initial HAp/β-TCP ratios of raw materials for the range of 0 wt% β-TCP, 21 wt% β-TCP, 34 wt% β-TCP and 59 wt% β-TCP, respectively. High-temperature treatment will lead to phase decomposition that results in a different ratio of β-TCP/HAp and a highly crystal-line, sintered porous bioceramic with a different rate of biodegradation (Park et al., 2009). However, the HAp/β-TCP ratio of 6/4 is commonly used in clinical applications; thus, an animal product was obtained for this study.

3.4. Cell viability of porous bioceramics

Fig. 7 shows the results of an indirect cytotoxicity test for the control groups against the porous bioceramic after incubation for 24 and 48 h. There were no statistically significant differences between the normal control, the negative control of Al_2O_3 and the bioceramic. Conversely, the viability of the phenol diluent positive control showed a tendency towards a severe decline after 24 and 48 h. These results indicated that our fabrication process could completely remove the PNM99:1 polymer and resulted in no cell toxicity effects for the pure porous calcium phosphate bioceramics. It is generally accepted that the in vitro cell-material interaction is a useful criterion in the evaluation of newly synthesized biomaterials.

3.5. In vivo experiments

3.5.1. Soft X-ray observation
Gross examination of the callus formation was performed using the X-ray photographs. Fig. 8(a1, b1) and (a2, b2) show X-ray images of the control group and the rhBMP-2 carrier group, respectively. All defects of both groups (a1, b1, a2, b2) had some scattered bridging callus formation between 6 weeks and 8 weeks, but there were still obvious gaps (white arrows) in the control group at the 6th week and 8th weeks. In contrast, the X-ray images of the 1-mm defect in the
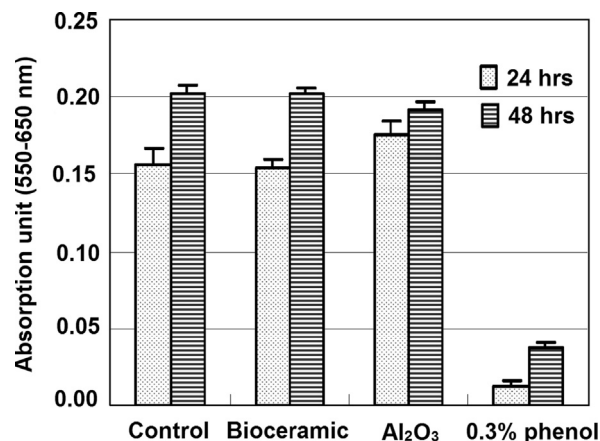

Fig. 7 – MTS assay of 3T3-E1 osteoblast-like cells was evaluated on different extract solutions of various samples for 24 and 48 h. Data are presented as the mean±SD (n=3).

femurs of the bioceramic spacer group and the bioceramic spacer with rhBMP-2 carriers group in Fig. 8(a3, b3) and (a4, b4) still showed an in situ bioceramic spacer at the 6th and 8th weeks, which was not present in the non-treated control. None of the X-ray micrographs of the samples after 6 weeks and 8 weeks showed good union, including those from the bioceramic spacer with rhBMP-2 carriers group. We supposed that the bioceramic scaffold was not absorbed completely within this short time period, and it was hard to differentiate the bone matrix within the scaffold. Therefore, histological images were needed to analyze the difference.

3.5.2. Histological analysis and bone tissue callus area calculation
In Fig. 8(a1) and (b1), a histological analysis of the control group was performed at the 6th and 8th weeks. We designed an atrophic non-union model in our control group. In this model, both bone ends were shrunken, and the fibrous tissue filled the defect. Additionally, the fissure joint between the fibrous tissue formed a pseudoarthrosis in Fig. 8(b1) (most severe form of arrest in fracture repair) according to the classification system reported by Allen et al. (Allen et al., 1980). In contrast, histological micrographs of the 1-mm defect in the femurs of the rhBMP-2 carrier group, bioceramic spacer group and bioceramic spacer with rhBMP-2 carriers groups in Fig. 8(a2, b2), (a3, b3) and (a4, b4), respectively, showed better callus formation both around the defect site and wrapping the bioceramic scaffold. At the 8th week
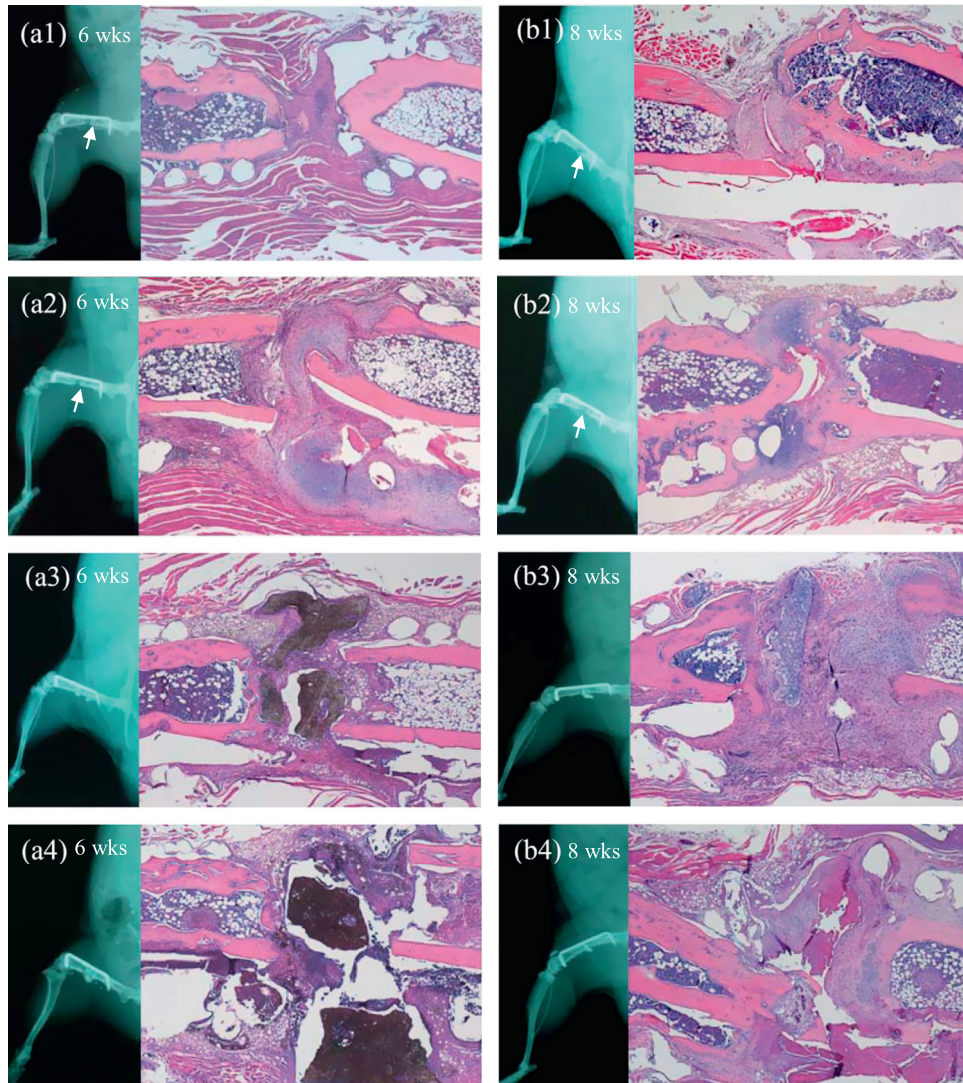
Fig. 8 – Radiography and histological study of one millimeter non-union Balb/C mouse model at 6 and 8 weeks after implantation of rhBMP-2 carriers only, HAp/β-TCP (6/4) bioceramic spacer and HAp/β-TCP (6/4) bioceramic spacer with rhBMP-2 carriers. (a1, b1: control group), (a2, b2: rhBMP-2 carriers group), (a3, b3: bioceramic spacer group) and (a4, b4: bioceramic spacer with rhBMP-2 carriers).

after surgery, the bioceramic spacer group and the bioceramic with rhBMP-2 carriers group had more calluses bridging the defect area around the scaffold than did the rhBMP-2 carriers group. We further used Image-Pro Plus to quantify the calcified callus in the H&E-stained histological sections matrix. The results showed that the percentages of bone callus formation in the rhBMP-2 carriers group, the bioceramic spacer group and the bioceramic spacer with rhBMP-2 carriers group were significantly better than those of the control group at 6 weeks and 8 weeks (Fig. 9). In addition, the results from the bioceramic spacer with rhBMP-2 carriers group were also significantly better than those of the rhBMP-2 carriers group at 8 weeks. The rhBMP-2 controlled-release profile results of our previous study showed an effective dose of greater than 20 ng/ml of constant rhBMP-2 release, which induced significant bone formation during the first one-week period in a bone graft model (Wang et al., 2009). However, that dose was unable to effectively treat atrophic

nonunion bone defects because of the lack of a scaffold that could provide an osteoconductive effect. Therefore, we supposed that the porous bioceramic of our samples could provide a good osteoconductive surface on which bone formation can occur. Moreover, quantification at 8 weeks indicates that the bioceramic spacer with rhBMP-2 carriers worked better than the bioceramic spacer after. We supposed that the dual effects of the bone growth factors of the osteoconductive bioceramic and the osteoinductive rhBMP-2 carriers should have better bone formation than other groups.

3.5.3. Immunostaining of bone tissue

After 6 weeks of treatment, the formation and growth of new blood vessels were obviously displayed, as observed using vWF staining of the endothelial tissue in the bioceramic spacer and the bioceramic spacer with rhBMP-2 carriers groups. Fig. 10 shows that the bioceramic spacer and

bioceramic spacer with rhBMP-2 carriers groups had more scattered brown-colored epithelium tissues in the defect area than did the control group at 6 and 8 weeks. The
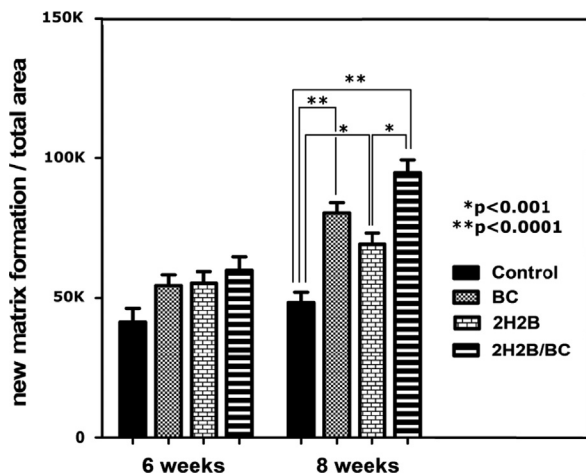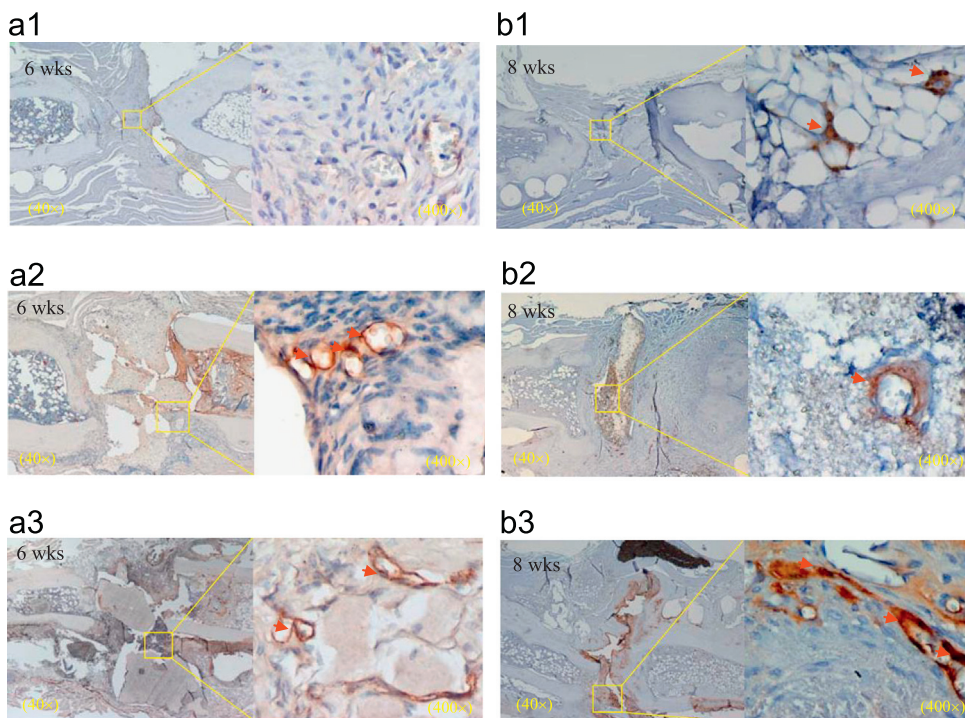

Fig. 9 – Histological quantification study of one millimeter non-union Balb/C mouse model at 6 and 8 weeks after implantation of rhBMP-2 carriers only, HAp/β-TCP (6/4) bioceramic spacer and HAp/β-TCP (6/4) bioceramic spacer with rhBMP-2 carriers by calculated the cell ingrowth into transplant bone. Data are presented as the mean ± SD ($n=6$). (Control: without any treatment, 2H2B: rhBMP-2 carriers group, BC: bioceramic spacer group, and 2H2B/BC: bioceramic spacer with rhBMP-2 carriers) (*$p<0.001$ and **$p<0.0001$ was compared to the control or compared between treatment groups.).

neovascularization represents the new vessel ingrowth, and this process can bring more bone marrow stromal cells to facilitate bone formation.

In our animal study, the callus formation around the bioceramic spacer and around the bioceramic spacer with rhBMP-2 carriers was significantly more than that of the control group at 6 weeks after implantation (Fig. 8). The histological results also showed that significant neovascularization was found in both the bioceramic spacer group and bioceramic spacer with rhBMP-2 carriers group 6 and 8 weeks after grafting, while that result was rarely observed in the control group (Fig. 10). The rhBMP-2 carrier group exhibited angiogenesis but was not better than the bioceramic spacer with rhBMP-2 carriers group. These results indicated that the osteoconductive effect of the HAp/β-TCP bioceramic spacer and the released effective osteoinductive dose of rhBMP-2 significantly stimulated new vessels that invaded around and into the ceramic scaffold cavities, which might help transport stem cells into the scaffold to facilitate bone regeneration. In the rhBMP-2 group, however, the large defect had no niche surface for new vessels to creep over even when stimulated by rhBMP-2. Consequently, the bone marrow stromal cells could not be transported to the defect area, which reasonably explains the fact that the rhBMP-2 group cannot work as well as in our previous study (Wang et al., 2009).

4. Conclusions

This study shows the successful synthesis of the reverse thermo-responsive copolymer of p(NiPAAm–MAA) by polymerization of

Fig. 10 – Immunohistochemistry study of one millimeter non-union Balb/C mouse model at 6 and 8 weeks after implantation of HAp/β-TCP (6/4) bioceramic spacer and HAp/β-TCP (6/4) bioceramic spacer with rhBMP-2 carriers and red arrows identify the incipient sites of blood vessels. (a1, b1(400 ×): control group), (a2, b2: bioceramic spacer group) and (a3, b3: bioceramic spacer with rhBMP-2 carriers). (For interpretation of the references to color in this figure legend, the reader is referred to the web version of this article.)

NiPAAm and MAA. Because the aqueous p(NiPAAm–MAA) is a reverse thermo-responsive hydrogel, which can shrink as the temperature increases, the compression function can be regarded as a cold isostatic pressing (CIP) effect to help densification of the ceramic during sintering. Few techniques for producing highly porous bioceramics with similar cancellous bone compression strength ($> \sim 5$ MPa) have been developed. The novel methods to introduce porosity into a bioceramic are mainly based on the admixture of a combustible reverse thermo-responsive hydrogel that burns away during sintering and on the air bubbles generated during the mixing process that leave free spaces in the resulting object. The optimal compressive strength and porosity of the porous bioceramics were examined between 6.8 and 4.1 MPa and 66.2% and 68.4% under 10–15 wt% PNM99:1 conditions. In addition, the HAp/β-TCP ratio of biphasic bioceramics can be adjusted to 7/3, 6/4, 4/6 and 3/7 during the 1200 °C sintering process. In animal studies, the results showed that none of the X-ray micrographs of the samples after 6 weeks and 8 weeks indicated good union, including those of the bioceramic spacer with rhBMP-2 carriers group. Histological micrographs of the 1-mm defect in femurs with the rhBMP-2 carrier group, the bioceramic spacer group and the bioceramic spacer with rhBMP-2 carriers group, however, appeared to have had better callus formation around the femur defect site. In the rhBMP-2 carriers only group, large bone defects were still unable to be effectively treated without any scaffold. The porous bioceramic scaffold possessed better osteoconductive ability than the rhBMP-2 carriers only group. The dual effects of bone growth factors from osteoconductive bioceramic and osteoinductive rhBMP-2 carriers can have better bone formation than other groups in addition to better callus formation and significant neovascularization. The use of porous bioceramic scaffolds with controlled release rhBMP-2 carriers to support bone growth shows a wealth of potential clinical applications for the treatment of non-union fractures.

Acknowledgments

Appendix A.   Supporting information

Supplementary data associated with this article can be found in the online version at http://dx.doi.org/10.1016/j.jmbbm.2013.06.009.

REFERENCES

Allen, H.L., Wase, A., Bear, W.T., 1980. Indomethacin and aspirin: effect of nonsteroidal anti-inflammatory agents on the rate of fracture repair in the rat. Acta Orthopaedica Scandinavica 51, 595–600.

Bauer, T.W., Muschler, G.F., 2000. Bone graft materials. An overview of the basic science. Clinical Orthopaedics and Related Research 371, 10–27.

Cui, Z., Lee, B.H., Vernon, B.L., 2007. New hydrolysis-dependent thermosensitive polymer for an injectable degradable system. Biomacromolecules 8, 1280–1286.

Daculsi, G., Laboux, O., Malard, O., Weiss, P., 2003. Current state of the art of biphasic calcium phosphate bioceramics. Journal of Materials Science: Materials in Medicine 14, 195–200.

Dong, J., Kojima, H., Uemura, T., Kikuchi, M., Tateishi, T., Tanaka, J., 2001. In vivo evaluation of a novel porous hydroxyapatite to sustain osteogenesis of transplanted bone marrow-derived osteoblastic cells. Journal of Biomedical Materials Research 57, 208–216.

Fan, X., Case, E.D., Ren, F., Shu, Y., Baumann, M.J., 2012. Part II: fracture strength and elastic modulus as a function of porosity for hydroxyapatite and other brittle materials. Journal of the Mechanical Behavior of Biomedical Materials 8, 99–110.

Feil, H., Bae, Y.H., Feijen, J., Kim, S.W., 1993. Effect of comonomer hydrophilicity and ionization on the lower critical solution temperature of N-isopropylacrylamide copolymers. Macromolecules 26, 2496–2500.

Fujishige, S., Kubota, K., Ando, I., 1989. Phase transition of aqueous solutions of poly(N-isopropylacrylamide) and poly (Nisopropylmethacrylamide). Journal of Physical Chemistry 93, 3311–3313.

Gan, T., Zhang, Y., Guan, Y., 2009. In situ gelation of P(NIPAM-HEMA) microgel dispersion and its applications as injectable 3D cell scaffold. Biomacromolecules 10, 1410–1415.

Gauthier, O., Bouler, J.M., Weiss, P., Bosco, J., Daculsi, G., Aguado, E., 1999. Kinetic study of bone ingrowth and ceramic resorption associated with the implantation of different injectable calcium-phosphate bone substitutes. Journal of Biomedical Materials Research 47, 28–35.

Han, Y., Li, J., Wei, Q., Tang, K., 2002. The effect of sintering temperatures on alumina foam strength. Ceramics International 28, 755–759.

Hench, L.L., Polak, J.M., 2002. Third-generation biomedical materials. Science 295, 1014–1017.

Heskins, M., Guillet, J.E., 1968. Solution properties of poly (N-isopropylacrylamide). Journal of Macromolecular Science, Part A. Pure and Applied Chemistry 2, 1441–1455.

Hirotsu, S., 1987. Phase transition of a polymer gel in pure and mixed solvent media. Journal of the Physical Society of Japan 56, 233–242.

Huglin, M.B., Liu, Y., Velada, J.L., 1997. Thermoreversible swelling behaviour of hydrogels based on N-isopropylacrylamide with acidic comonomers. Polymer 38, 5785–5791.

Hulbert, S.F., Young, F.A., Mathews, R.S., Klawitter, J.J., Talbert, C.D., Stelling, F.H., 1970. Potential of ceramic materials as permanently implantable skeletal prostheses. Journal of Biomedical Materials Research 4, 433–456.

Kretlow, J.D., Mikos, A.G., 2007. Review: mineralization of synthetic polymer scaffolds for bone tissue engineering. Tissue Engineering 13, 927–938.

Komlev, V.S., Barinov, S.M., 2002. Porous hydroxyapatite ceramics of bimodal pore size distribution. Journal of Materials Science: Materials in Medicine 13, 295–299.

Langer, R., Vacanti, J.P., 1993. Tissue engineering. Science 260, 920–926.

Lord, C.F., Gebhardt, M.C., Tomford, W.W., Mankin, H.J., 1988. Infection in bone allografts. Incidence, nature, and treatment. Journal of Bone and Joint Surgery, American Volume 70, 369–376.

Muscolo, D.L., Ayerza, M.A., Aponte-Tinao, L.A., 2006. Massive allograft use in orthopedic oncology. Orthopedic Clinics of North America 37, 65–74.

Otake, K., Inomata, H., Konno, M., Saito, S., 1990. Thermal analysis of the volume phase transition with N-isopropylacrylamide gels. Macromolecules 23, 283–289.

Park, J.C., Lim, H.C., Sohn, J.Y., Yun, J.H., Jung, U.W., Kim, C.S., et al., 2009. Bone regeneration capacity of two different macroporous biphasic calcium materials in rabbit calvarial defect. Journal of Korean Academy of Periodontology 39, 223–230.

Rafie, F., Pashapour, T., Jafari, B., Javadzadeh, Y., Davaran, S., 2012. Preparation and in-vitro release of smart nanoparticles containing indomethacin for use in ophthalmic anti inflammatory formulations. Journal of Controlled Release 1, 64–69.

Ramay, H.R., Zhang, M., 2003. Preparation of porous hydroxyapatite scaffolds by combination of the gel-casting and polymer sponge methods. Biomaterials 24, 3293–3302.

Rezwan, K., Chen, Q.Z., Blaker, J.J., Boccaccini, A.R., 2006. Biodegradable and bioactive porous polymer/inorganic composite scaffolds for bone tissue engineering. Biomaterials 27 3413–2431.

Rust, A.C., Manga, M., 2002. Effects of bubble deformation on the viscosity of dilute suspensions. Journal of Non-Newtonian Fluid Mechanics 104, 53–63.

Silber, J.S., Anderson, D.G., Daffner, S.D., Brislin, B.T., Leland, J.M., Hilibrand, A.S., et al., 2003. Donor site morbidity after anterior iliac crest bone harvest for single-level anterior cervical discectomy and fusion. Spine 28, 134–139.

Solchaga, L.A., Dennis, J.E., Goldberg, V.M., Caplan, A.I., 1999. Hyaluronic acid-base polymers as cell carriers for tissue-engineerined repair of bone and cartilage. Journal of Orthopaedic Research 17, 205–213.

Solis, F.J., Weiss-Malik, R., Vernon, B., 2005. Local monomer activation model for phase behavior and calorimetric properties of LCST gel forming polymers. Macromolecules 38, 4456–4464.

Stevens, M.M., 2008. Biomaterials for bone tissue engineering. Materials Today 11, 18–25.

Tadic, D., Beckmann, F., Schwarz, K., Epple, M., 2004. A novel method to produce hydroxyapatite objects with interconnecting porosity that avoids sintering. Biomaterials 25, 3335–3340.

Tampieri, A., Celotti, G., Sprio, S., Delcogliano, A., Franzese, S., 2001. Porosity-graded hydroxyapatite ceramics to replace natural bone. Biomaterials 22, 1365–1370.

Tian, P., Wu, Q., Lian, K., 2008. Preparation of temperature- and pH-sensitive, stimuli-responsive poly(N-isopropylacrylamide-co-methacrylic acid) nanoparticles. Journal of Applied Polymer Science 108, 2226–2232.

Uchida, A., Nade, S., McCartney, E., Ching, W., 1985. Bone ingrowth into three different porous ceramics implanted into the tibia of rats and rabbits. Journal of Orthopaedic Research 3, 65–77.

Yamada, S., Heymann, D., Bouler, J.M., Daculsi, G., 1997. Osteoclastic resorption of calcium phosphate ceramics with different hydroxyapatite/beta-tricalcium phosphae retios. Biomaterials 18, 1037–1041.

Wang, C.K., Ho, M.L., Wang, G.J., Chang, J.K., Chen, C.H., Fu, Y.C., et al., 2009. Controlled-release of rhBMP-2 carriers in the regeneration of osteonecrotic bone. Biomaterials 30, 4178–4186.

Zhang, X.Z., Wu, D.Q., Chu, C.C., 2004. Synthesis, characterization and controlled drug release of thermosensitive IPN-PNIPAAm hydrogels. Biomaterials 25, 3793–3805.